Photoelectron Spectroscopy of Doubly and Singly Charged Group VIB Dimetalate Anions: $M_2O_7^{2-}$, $MM'O_7^{2-}$, and $M_2O_7^{-}$ (M, M′ = Cr, Mo, W)

Hua-Jin Zhai,[†] Xin Huang,[†] Tom Waters,[†] Xue-Bin Wang,[†] Richard A. J. O'Hair,[‡] Anthony G. Wedd,[‡] and Lai-Sheng Wang*,[†]

Department of Physics, Washington State University, 2710 University Drive, Richland, Washington 99354, W. R. Wiley Environmental Molecular Sciences Laboratory and Chemical Sciences Division, Pacific Northwest National Laboratory, P.O. Box 999, MS K8-88, Richland, Washington 99352, and School of Chemistry, The University of Melbourne, Victoria, Australia, 3010

Received: September 10, 2005

We produced both doubly and singly charged Group VIB dimetalate species—$M_2O_7^{2-}$, $MM'O_7^{2-}$, and $M_2O_7^{-}$ (M, M′ = Cr, Mo, W)—using two different experimental techniques (electrospray ionization for the doubly charged anions and laser vaporization for the singly charged anions) and investigated their electronic and geometric structures using photoelectron spectroscopy and density functional calculations. Distinct changes in the electronic and geometric structures were observed as a function of the metal and charge state. The electron binding energies of the heteronuclear dianions $MM'O_7^{2-}$ were observed to be roughly the average of those of their homonuclear counterparts ($M_2O_7^{2-}$ and $M'_2O_7^{2-}$). Density functional calculations indicated that $W_2O_7^{2-}$, $W_2O_7^{-}$, and W_2O_7 possess different ground-state structures: the dianion is highly symmetric (D_{3d},$^1A_{1g}$) with a single bridging oxo ligand, the monoanion is a doublet (C_1, ^2A) with two bridging oxo ligands and a radical terminal oxo ligand, whereas the neutral is a singlet (C_1, ^1A) with two bridging oxo ligands and a terminal peroxo ligand. The combined experimental and theoretical study provides insights into the evolution of geometric and electronic structures as a function of charge state. The clusters identified might provide insights into the possible structures of reactive species present in early transition-metal oxide catalysts that are relevant to their reactivity and catalytic function.

1. Introduction

Polyoxometalate anions continue to attract research interest because of their diverse applications in fields such as catalysis, biochemistry, medicine, and solid-state devices.[1] Their high thermal stability, Brönsted acidity, and ability to undergo multiple reversible reductions make them ideal candidates for acid−base, redox, and bifunctional catalysis. In addition, a major impetus in their study has been their application as soluble metal-oxides and their possible role as molecular models for metal-oxide surfaces that are important in many catalytic processes. Such oxides or supported oxides of chromium, molybdenum, and tungsten are important in a variety of catalytic processes that involve oxidation, dehydrogenation, and isomerization reactions.[2] The properties of these oxides differ significantly with variation of the metal: chromium oxides are usually used for their redox properties, whereas tungsten oxides seem better suited for acid−base or isomerization reactions.[2] To this end, mixed oxides containing two of the components chromium, molybdenum, or tungsten have been tested, to combine the favorable properties of the two component species.[3]

Dimetalate dianions, which consist of two corner-sharing tetrahedral MO_4 units, can be considered as the simplest polyoxoanions. Dichromate ($Cr_2O_7^{2-}$) has been well-characterized in aqueous solution and crystalline compounds.[4,5] Discrete dimolybdate anions ($Mo_2O_7^{2-}$) have been prepared from nonaqueous solutions and structurally characterized.[6,7] A few other isostoichiometric compounds have been reported, but these consist of chains of either MoO_6 octahedra or MoO_5 trigonal bipyramidal units.[8,9] The detailed geometric structures of the $Cr_2O_7^{2-}$ and $Mo_2O_7^{2-}$ dianions have been observed to vary as a function of counterion,[4−7] indicating that their intrinsic structural properties are subject to significant perturbations that are due to changes of crystal fields and counterions. In contrast, discrete $W_2O_7^{2-}$ dianions have not been isolated, despite synthetic efforts,[10] and although stoichiometric tungsten oxides of the general formula $A_2W_2O_7$ (where A is a cation, often an alkali metal) are known, these are comprised of chains of corner- and edge-shared WO_6 octahedral and WO_4 tetrahedral units.[8,11]

Dichromate and dimolybdate dianions have been observed in the gas phase using electrospray ionization (ESI), and are known to be stable gas-phase dianions.[12,13] In addition, the ditungstate dianion can be generated by electrospraying solutions of tungstate and has also been observed to be a stable gas-phase dianion.[13,14] More recently, heteronuclear dianions $MM'O_7^{2-}$ (M, M′ = Cr, Mo, W) were generated similarly in the gas phase from solutions containing two of the species CrO_4^{2-}, MoO_4^{2-}, or WO_4^{2-}.[15] With regard to singly charged anions, $Cr_2O_7^{-}$ and $W_2O_7^{-}$ have been generated by laser vaporization and detected by mass spectrometry.[16] These represent the one-electron oxidized forms of dichromate and ditungstate. To our knowledge, none of the $M_2O_7^{2-}$, $MM'O_7^{2-}$, and $M_2O_7^{-}$ (M, M′ = Cr, Mo, W) species have been studied spectroscopically in the gas phase. A few theoretical studies on the electronic and geometric structure of the dianions $M_2O_7^{2-}$ are available.[17,18]

* To whom correspondence should be addressed. E-mail: ls.wang@pnl.gov.
[†] Washington State University and Pacific Northwest National Laboratory.
[‡] The University of Melbourne.

10.1021/jp055122y CCC: $30.25
Published on Web 11/01/2005

We have been interested in developing cluster models for oxide surfaces and catalysts,[13,15,19−21] in which we combine photoelectron spectroscopy (PES) and theoretical calculations to characterize novel oxide cluster species in the gas phase and to obtain possible mechanistic insight into the complicated surface structures and catalytic processes. Indeed, gas-phase cluster studies have recently emerged as an alternative approach toward mechanistic understanding of catalysis at the molecular level.[13,15,19−24] In a recent study on mononuclear tungsten and molybdenum oxide clusters (MO_n^-, where M = Mo or W and n = 3−5), we identified unique W−O$^\bullet$ and $O_2^{-\bullet}$ radical characters in WO_4 and WO_5, respectively.[19] More recently, we investigated the electronic structure of two larger polyoxoanions, $Mo_6O_{19}^{2-}$ and $W_6O_{19}^{2-}$, that were transferred to the gas phase by ESI and then investigated by PES.[20] With regard to reactivity, recent multistage mass spectrometry experiments on a series of dimetalate anions have demonstrated two gas-phase catalytic cycles for the partial oxidation of methanol to formaldehyde. The reactions of these catalytic cycles seem to be similar to those occurring in a related condensed-phase industrial process.[13,15]

In the current work, we report a combined PES and density functional theory (DFT) study on the electronic and structural properties of a series of dimetalate molecules in their dianionic, monoanionic, and neutral states: $M_2O_7^{2-}$, $MM'O_7^{2-}$, $M_2O_7^-$, and M_2O_7 (M, M′ = Cr, Mo, W). The $M_2O_7^{2-}$ and $MM'O_7^{2-}$ dianions and the $M_2O_7^-$ monoanions were produced by the ESI and laser vaporization techniques, respectively. Photodetachment experiments were performed for each of these species at various photon energies up to 157 nm (7.866 eV). Molecular orbital analyses are used to explain the trend of the observed spectra for the dianions and obtain insight into their electronic structure variation with the metals. Detailed DFT calculations have been performed on the W_2O_7 species in all three charge states, and their global minimum structures are observed to be dependent on the charge states.

2. Experimental and Theoretical Methods

2.1. Photoelectron Spectroscopy of $M_2O_7^{2-}$ and $MM'O_7^{2-}$ (M, M′ = Cr, Mo, W) Dianions Using Electrospray Ionization. The design and operation of the ESI−PES apparatus have been described in detail previously,[25] and only a brief description is provided here. The dichromate and dimolybdate dianions $Cr_2O_7^{2-}$ and $Mo_2O_7^{2-}$ were generated by electrospraying ∼10^{-3} M solutions of $(Bu_4N)_2[Cr_2O_7]$ and $(Bu_4N)_2[Mo_2O_7]$, respectively, in CH_3CN solvent. The ditungstate dianion $W_2O_7^{2-}$ was generated using an ∼10^{-3} M solution of $(Bu_4N)_2[WO_4]$ in CH_3CN, and the $W_2O_7^{2-}$ dianion was presumably formed by the condensation of two mononuclear centers. The mass signal intensity for $W_2O_7^{2-}$ was extremely weak, which was consistent with the fact that it has not been isolated in the condensed phase. The heteronuclear dianions $MM'O_7^{2-}$ were generated by electrospraying ∼10^{-3} M CH_3CN solutions that contained two of the salts $(Bu_4N)_2[CrO_4]$, $(Bu_4N)_2[MoO_4]$, or $(Bu_4N)_2[WO_4]$, and they were presumably formed by the condensation of two different mononuclear centers. Sample solutions were sprayed from a 0.01-mm-diameter syringe needle biased at −2.2 kV into a desolvation capillary that was maintained at ∼70 °C. Negative ions emerging from the capillary were transferred into a quadrupole ion trap and accumulated for a period of 100 ms before being passed into the extraction zone of a time-of-flight (TOF) mass spectrometer. The anions of interest were mass-selected and decelerated before being intercepted by a laser beam in the detachment zone of a magnetic-bottle PES analyzer. Three detachment photon energies were used in the current experiment: 266 nm (4.661 eV) from a Nd:YAG laser, 193 nm (6.424 eV) from an excimer laser, and 157 nm (7.866 eV) from an excimer laser. Photoelectrons were collected at almost 100% efficiency by the magnetic bottle and analyzed in a 4-m-long photoelectron TOF tube. Photoelectron TOF spectra were converted to kinetic energy spectra and calibrated with the known spectra of I^- and O^-. Binding energy spectra were calculated by subtracting the kinetic energy spectra from the known photon energies. The electron energy resolution ($\Delta E/E$) is estimated to be ∼2% (fwhm), i.e., ∼10 meV for 0.5 eV electrons, as measured from the spectra of I^- at 355 nm.

2.2. Photoelectron Spectroscopy of $M_2O_7^-$ (M = Cr, Mo, W) Monoanions Using Laser Vaporization. PES of the monoanions $M_2O_7^-$ (M = Cr, Mo, W) was performed using a magnetic-bottle PES apparatus that was equipped with a laser vaporization supersonic cluster source.[26] Briefly, $M_mO_n^-$ cluster anions were produced by laser vaporization of the respective Group VIB metal target in the presence of a helium carrier gas seeded with 0.5% O_2, and were mass-analyzed using a TOF mass spectrometer. The $M_2O_7^-$ species were each mass-selected and decelerated before being photodetached. Because of their extremely high electron binding energies, only two detachment photon energies from an excimer laser were used in the current study: 193 nm (6.424 eV) (ArF) and 157 nm (7.866 eV) (F_2). Photoelectrons were collected at almost 100% efficiency by the magnetic bottle and analyzed in a 3.5-m-long electron flight tube. The photoelectron spectra were calibrated using the known spectrum of Rh^-, and the energy resolution of the apparatus was $\Delta E_k/E_k$ ∼ 2.5% (that is, ∼25 meV for 1-eV electrons).

2.3. Density Functional Calculations. Theoretical calculations were performed at the DFT level using the B3LYP hybrid functional.[27] The search for the global minima was performed using analytical gradients with the Stuttgart 14-valence electron pseudo-potentials and basis sets[28] augmented with two f-type and one g-type polarization functions, as recommended by Martin and Sundermann[29] for the metal atoms and the aug-cc-pVTZ basis set for oxygen.[30] Scalar relativistic effects (i.e., the mass-velocity and Darwin effects) were taken into account via the quasi-relativistic pseudo-potentials. Because we were mainly interested in explaining the experimental PES data, spin−orbit coupling effects were neglected. Our previous study on tungsten oxide species showed that spin−orbit coupling effects would shift the orbital energies by, at most, a few tenths of an electron volt,[20] which should not affect spectral assignments. Vibrational frequencies were calculated at the same level of theory to verify the nature of the stationary points. Vertical electron detachment energies (VDEs) were calculated using the generalized Koopman's theorem,[31] by adding a correction term to the eigenvalues of the anions. The correction term was estimated by the relation $\delta E = E_1 - E_2 - \epsilon_{HOMO}$, where E_1 and E_2 are the total energies of the anion and neutral, respectively, in their ground electronic states at the anion equilibrium geometry and ϵ_{HOMO} corresponds to the eigenvalue of the highest occupied molecular orbital (HOMO) of the anion. The extra-fine integration grid was used to obtain accurate DFT results. Calculations were performed using the NWChem 4.6 program at the Molecular Science Computing Facility located at the Environmental Molecular Sciences Laboratory.[32] Three-dimensional contours of the calculated Kohn−Sham orbitals were generated using the Extensible Computational Chemistry Environment (Ecce) software.[33]

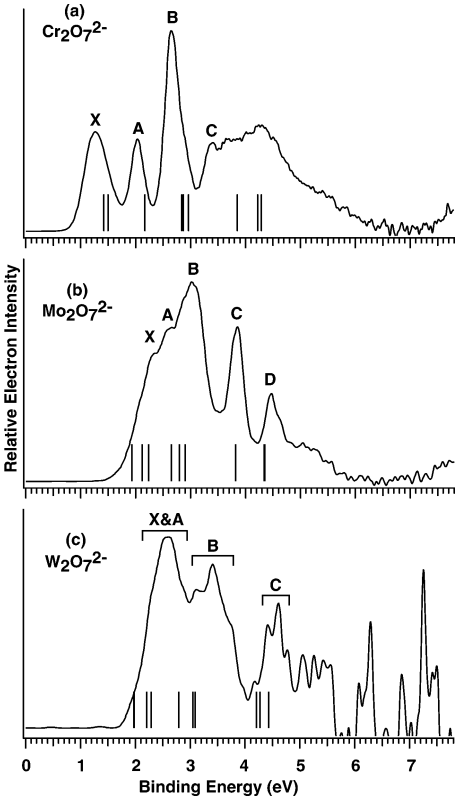

Figure 1. Photoelectron spectra of (a) $Cr_2O_7^{2-}$, (b) $Mo_2O_7^{2-}$, and (c) $W_2O_7^{2-}$ at 157 nm (7.866 eV). Vertical bars represent the vertical detachment energies (VDEs) computed using the generalized Koopman's theorem (see text).

3. Experimental Results

3.1. Homonuclear Dianions $M_2O_7^{2-}$ (M = Cr, Mo, W). PES spectra for $M_2O_7^{2-}$ (M = Cr, Mo, W) at 157 nm are illustrated in Figure 1. Spectra were also obtained at 193 and 266 nm, and they are included in the Supporting Information (see Figures S1−S3). The observed adiabatic detachment energies (ADEs) for the ground-state transition and the VDEs for the first few PES bands are given in Table 1. All observed features and comparison with calculations are given in the Supporting Information (see Table S1). Because of the lack of vibrational resolution, ADEs were estimated by drawing a straight line along the leading edge of the threshold band and then adding the instrumental resolution to the intersection with the binding energy axis. The VDE of each band was measured from the peak maximum. Many of the detachment features reported here seem to result from multiple overlapping transitions, so the experimental VDEs should be considered as an average of these transitions in those cases.

Three well-resolved bands (denoted as X, A, and B) are apparent at lower binding energies for $Cr_2O_7^{2-}$ (see Figure 1a and Figure S1), with a series of overlapping features at higher binding energies. The ADE and VDE of band X were estimated to be 1.10 and ∼1.3 eV, respectively (see Table 1). The PES data of $Mo_2O_7^{2-}$ (see Figure 1b and Figure S2) seem to be quite different from that of $Cr_2O_7^{2-}$ and are very congested near the threshold that is composed of at least three bands (X, A, B). Two sharper features (C, D) are displayed at higher binding energies. The ADE and VDE of band X were estimated to be 1.88 and ∼2.2 eV, respectively (Table 1), which are significantly higher compared to those for $Cr_2O_7^{2-}$.

The spectra of $W_2O_7^{2-}$ (Figure 1c and Figure S3) were of poorer quality, because of the considerably weaker mass intensity of $W_2O_7^{2-}$. Similar to that of $Mo_2O_7^{2-}$, the spectra of $W_2O_7^{2-}$ are also rather congested near the threshold (X&A, B). There are no real signals beyond 5.5 eV: the spikes displayed on the high binding energy side were noise that was due to imperfect background subtraction. The ADE and VDE of band X for $W_2O_7^{2-}$ were estimated as 2.10 and 2.3 eV, respectively (see Table 1), which are slightly higher values than those for $Mo_2O_7^{2-}$.

TABLE 1: Observed Adiabatic Detachment Energies (ADEs) and Vertical Detachment Energies (VDEs) from the Photoelectron Spectra of Homonuclear and Heteronuclear Dianions, $M_2O_7^{2-}$ and $MM'O_7^{2-}$ (M, M′ = Cr, Mo, W)

species	observed feature	ADE[a,b] (eV)	VDE[b,c] (eV)
$Cr_2O_7^{2-}$	X	1.10 (5)	∼1.3
	A		2.04 (5)
	B		2.65 (5)
$Mo_2O_7^{2-}$	X	1.88 (7)	∼2.2
	A		∼2.5
	B		3.05 (5)
$W_2O_7^{2-}$	X	2.10 (7)	∼2.3
	A		∼2.6
	B		3.0−3.6
$CrMoO_7^{2-}$	X	1.56 (7)	1.85 (5)
	A		2.24 (5)
$CrWO_7^{2-}$	X	1.64 (7)	1.94 (4)
	A		2.39 (5)
$MoWO_7^{2-}$	X	1.92 (8)	2.40 (5)
	A		2.65 (5)

[a] Also represents the electron affinity of the corresponding $M_2O_7^-$ monoanion species. [b] Numbers in parentheses represent the experimental uncertainties in the last digit. [c] Observed bands may arise from multiple transitions; in those cases, the estimated VDEs should be considered to be an average of these transitions.

3.2. Heteronuclear Dianions $MM'O_7^{2-}$ (M, M′ = Cr, Mo, W). The 157-nm spectra for the three heteronuclear $MM'O_7^{2-}$ dianions are shown in Figure 2, and the 193 and 266 nm data are included in the Supporting Information (see Figures S4−S6). The spectra for these species seemed to be qualitatively more complex than those of their homonuclear counterparts. The ground-state ADEs for $CrMoO_7^{2-}$, $CrWO_7^{2-}$, and $MoWO_7^{2-}$ were estimated to be 1.56, 1.64, and 1.92 eV, respectively, whereas the corresponding VDEs were measured as 1.85, 1.94, and 2.40 eV (see Table 1).

3.3. $M_2O_7^-$ (M = Cr, Mo, W). The photoelectron spectra of the three homonuclear monoanions $M_2O_7^-$ are displayed in Figure 3, and the obtained ADEs and VDEs are given in Table 2. The electron binding energies for all these species are extremely high and, except for $Cr_2O_7^-$, the spectra could only be obtained at 157 nm. We were able to obtain the spectrum of $Cr_2O_7^-$ at 193 nm, which is given in the inset in Figure 3a. The lower photon energy spectrum shows that the X band is much better resolved. A weak tail (X′) was also observed in the 193-nm spectrum of $Cr_2O_7^-$ at lower binding energies, probably due to a weak isomer. Three well-separated PES bands (X, A, B) were observed for $Cr_2O_7^-$. The 193-nm spectrum yielded an ADE and VDE for the X band as 5.57 and 5.90 eV, respectively (see Table 2).

The overall spectral patterns of $Mo_2O_7^-$ and $W_2O_7^-$ seem to be similar: both consist of a broad band near the threshold (X, A) and a well-separated band (B) at higher binding energies. The electron binding energies for $Mo_2O_7^-$ and $W_2O_7^-$ are considerably higher relative to $Cr_2O_7^-$. We estimated the ground-state ADEs/VDEs to be ∼6.3/∼6.5 for $Mo_2O_7^-$ and ∼6.5/∼6.7 eV for $W_2O_7^-$ (see Table 2). The spectral changes

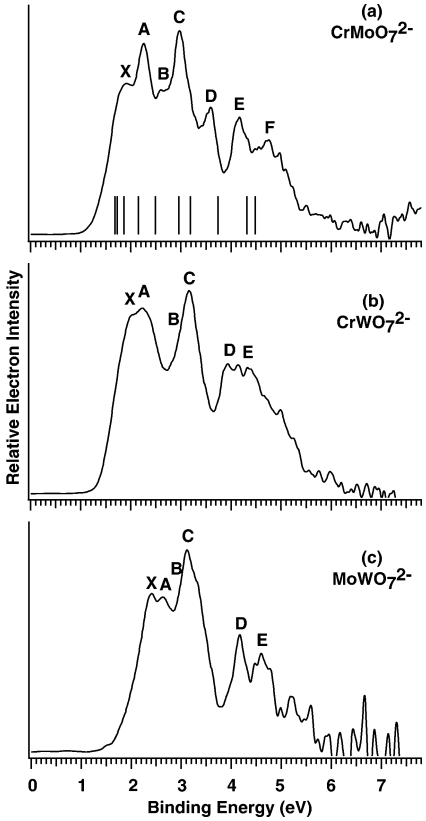

Figure 2. Photoelectron spectra of (a) $CrMoO_7^{2-}$, (b) $CrWO_7^{2-}$, and (c) $MoWO_7^{2-}$ at 157 nm. Vertical bars in panel a represent VDEs computed using the generalized Koopman's theorem (see text).

from $Cr_2O_7^-$ to its heavier congeners are similar to the changes in the corresponding dianions (see Figure 1).

4. Theoretical Results

4.1. Dianions $M_2O_7^{2-}$ (M = Cr, Mo, W) and $CrMoO_7^{2-}$. Previous theoretical studies based on Hartree−Fock (HF) and DFT have explored the structures of the $M_2O_7^{2-}$ dianions (M = Cr, Mo, W).[17,18] These studies suggested several different conformers with very similar energies involving both bent and linear M−O−M bridging units, as well as staggered and eclipsed conformations. The overall data are consistent with the notion that bending of the M−O−M unit and rotation of the MO_3 units are extremely facile. The present calculations were aimed at the VDEs to compare with the PES data and were conducted under D_{3d} symmetry for $M_2O_7^{2-}$ (M = Cr, Mo, W) with a linear bridging oxo unit and staggered MO_3 units. Although other conformers might also represent local minima, the precise choice of conformation is unlikely to affect their electronic structure significantly and should not affect the interpretation of the experimental results. The D_{3d} conformers were chosen for simplicity and consistency. Calculations were also performed for the representative heteronuclear species $CrMoO_7^{2-}$ under the equivalent C_{3v} symmetry. The calculated VDEs are shown in Figures 1 and 2 as vertical bars for comparison with the experimental data. The numerical data are collected in Tables S1 and S2 in the Supporting Information. We will focus our discussion below on the tungsten species. For simplicity, in the following presentation, O_t represents the terminal oxygen and O_b represents the bridging oxygen. The ground state of $W_2O_7^{2-}$ (**1**) is closed shell (D_{3d}, $^1A_{1g}$) with two corner-sharing tetrahedra joined at a single bridging oxo. Terminal and bridging bond lengths are 1.760 and 1.920 Å, respectively (Figure 4). The D_{3d} $W_2O_7^{2-}$ (**1**) conformation is consistent with previous calculations.[17,18]

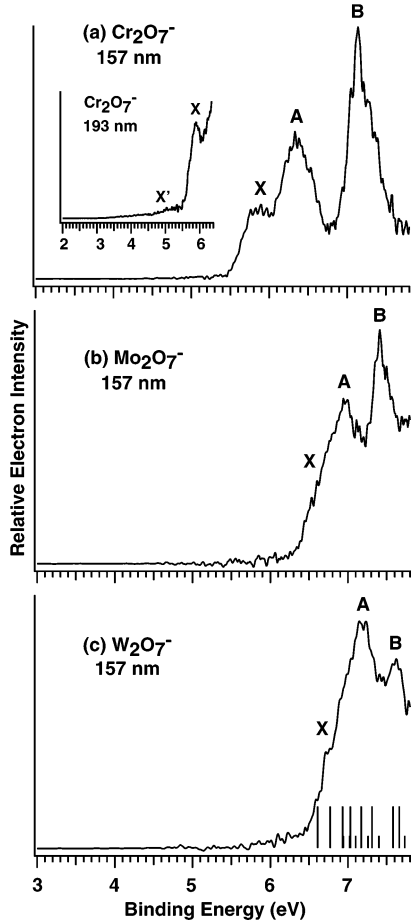

Figure 3. Photoelectron spectra of (a) $Cr_2O_7^-$, (b) $Mo_2O_7^-$, and (c) $W_2O_7^-$ at 157 nm. The inset in panel a shows the spectrum of $Cr_2O_7^-$ at 193 nm. The longer and shorter vertical bars in panel c represent VDEs to triplet and singlet final states, respectively, computed using the generalized Koopman's theorem (see text).

TABLE 2: Observed Adiabatic Detachment Energies (ADEs) and Vertical Detachment Energies (VDEs) from the Photoelectron Spectra of $M_2O_7^-$ (M = Cr, Mo, W)

species	feature	ADE[a,b] (eV)	VDE[b,c] (eV)
$Cr_2O_7^-$	X	5.57 (5)	5.90 (3)
	A		6.34 (5)
	B		7.14 (3)
$Mo_2O_7^-$	X	∼6.3	∼6.5
	A		6.97 (5)
	B		7.41 (3)
$W_2O_7^-$	X	∼6.5	∼6.7
	A		∼7.2
	B		7.62 (5)

[a] Also represents the electron affinity of the corresponding M_2O_7 neutral species. [b] Numbers in parentheses represent the experimental uncertainties in the last digit. [c] Observed bands may arise from multiple transitions, so the quoted VDEs should be considered to be an average of these transitions.

4.2. $W_2O_7^-$ and W_2O_7. Our theoretical effort has been mainly directed at the neutral and singly charged W−O systems, because very little is known about them. We performed an extensive search for their global minimum structures. The optimized ground-state geometries of $W_2O_7^-$ and W_2O_7 and selected low-lying isomers, along with their relative energies, are presented in Figure 4. Several structural isomers were identified for $W_2O_7^-$ (**2a**−**c**). The dibridged structure **2a** (C_1,

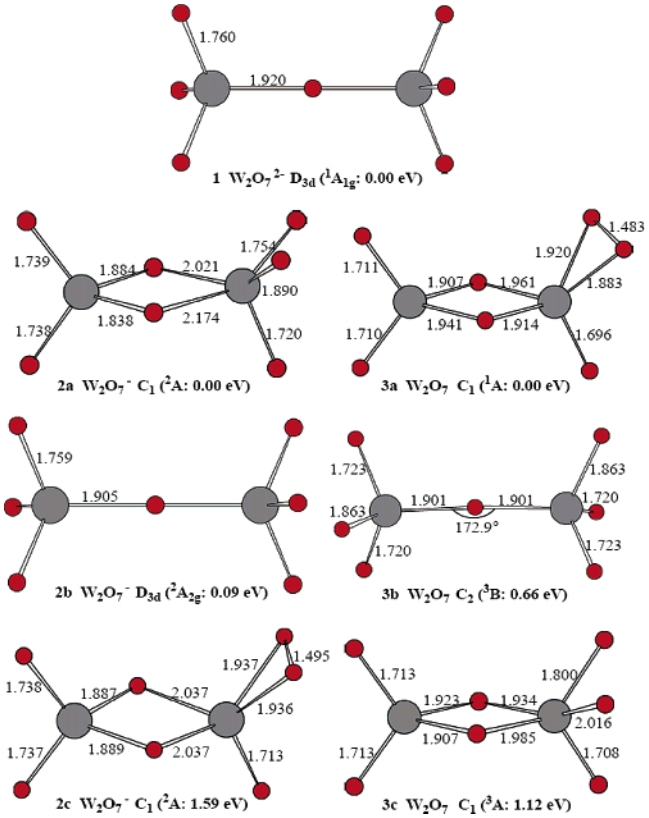

Figure 4. Optimized structures and their relative energies for $W_2O_7^{2-}$ (**1**), $W_2O_7^-$ (**2a**−**c**), and W_2O_7 (**3a**−**c**).

^{2}A) is predicted as the global minimum, whereas the D_{3d} isomer (**2b**), which is similar to the D_{3d} dianion $W_2O_7^{2-}$, is slightly higher in energy (by only 0.09 eV). A third isomer, **2c** (C_1, ^{2}A), with a peroxo ligand was located at much higher energy, by 1.59 eV above the global minimum. The two bridging oxo ligands in the ground-state structure **2a** exhibit significantly different W−O_b distances, which is consistent with the inequivalent tungsten sites to which they are coordinated. The unpaired electron in **2a** is localized on the terminal oxygen with the longest W−O bond length of 1.890 Å.

A similar set of structural isomers is located for neutral W_2O_7, but their stabilities are quite different. The dibridged structure with a peroxo O_2 **3a** (C_1, ^{1}A) is overwhelmingly favored as the ground state for W_2O_7, whereas the structure **3c** (C_1, ^{3}A), similar to the ground-state structure of $W_2O_7^-$, is much higher in energy in the neutral (by 1.12 eV). The monobridged isomer **3b** (C_2, ^{3}B) is located 0.66 eV above the ground state. The bridging oxo ligand of this isomer is slightly bent ($\angle WO_bW = 172.9°$), in contrast to the linear arrangement found for the monoanion and dianion (**1**, **2b**).

We also computed the VDEs for the global minimum structure of $W_2O_7^-$. These values are plotted as vertical bars in Figure 3c and are also given in Table S3 in the Supporting Information.

5. Comparison of Experimental Data with Theoretical Calculations

The computed VDE spectra for the homonuclear dianions $M_2O_7^{2-}$ (M = Cr, Mo, W) are plotted as vertical bars in Figure 1 and are compared with experimental VDEs in Table S1 in the Supporting Information. The agreement between the calculated VDE patterns and the experimental spectra is very good. As shown in Table S1, the X band for $Cr_2O_7^{2-}$, which is relatively broad, in fact corresponds to three detachment channels (a_{2g}, a_{1u}, e_u) with very similar calculated VDEs at 1.42, 1.42, and 1.50 eV, respectively. Band A corresponds to detachment from the e_g orbital with a computed VDE of 2.17 eV, compared with the experimental VDE of 2.04 eV. The relatively narrow band is consistent with the single detachment channel for this transition. Following an energy gap, three closely lying detachment channels (a_{2u}, e_u, a_{1g}) with calculated VDEs at 2.84, 2.87, and 2.96 eV were obtained, in excellent agreement with the broad and intense band B. Following another energy gap, more closely lying detachment channels were computed, corresponding to the observed band C and the higher detachment features. The computed VDEs for $Mo_2O_7^{2-}$ and $W_2O_7^{2-}$ are also consistent with the PES data (see Figure 1 and Table S1). In particular, the first VDE, predicted as 1.42 eV → 1.93 eV → 1.97 eV from Cr to W (see Table S1), clearly match the experimental trend of 1.3, 2.2, and 2.3 (see Table 1).

The theoretical data for the heteronuclear species $CrMoO_7^{2-}$ is compared with experimental data in Figure 2a and Table S2 in the Supporting Information. The predicted VDE of 1.68 eV is approximately the average of those for $Cr_2O_7^{2-}$ and $Mo_2O_7^{2-}$, in agreement with the experimental observation. The lower symmetry of $CrMoO_7^{2-}$ seems to make the spectral pattern more complex, and this increased complexity was also borne out by the calculations (see Figure 2a).

For the monoanions $M_2O_7^-$ (M = Cr, Mo, W), the observed ADEs follow the similar trend (5.57 eV → ∼6.3 eV → ∼6.5 eV from Cr to W) as that for the dianions, with a significant increase from Cr to Mo, but similar values are observed for Mo and W. Theoretical calculations were focused on the W species and the calculated VDEs for the lowest-energy structure of $W_2O_7^-$ are compared with the PES data in Figure 3c and Table S3 in the Supporting Information. The valence molecular orbitals of $W_2O_7^-$ are dominated by O 2p lone pairs and a very high density of electronic transitions was computed, in good agreement with the broad and congested photoelectron spectrum. The calculated first VDE (6.61 eV) for the **2a** global minimum is in good agreement with the extremely high VDE observed experimentally for $W_2O_7^-$ (∼6.7 eV). Note that the isomers **2b** and **2c** (Figure 4) would yield much lower VDEs, clearly disagreeing with the experimental observation.

6. Discussion

6.1. Intramolecular Coulomb Repulsion and the Repulsive Coulomb Barrier (RCB) in the Doubly Charged Anions $M_2O_7^{2-}$ and $MM'O_7^{2-}$. Intramolecular coulomb repulsion between the excess charges in multiply charged anions has a tendency to destabilize these species, significantly reducing their electronic binding energies and thermodynamic stability in the gas phase. This can be clearly seen by comparing the PES spectra of the dianions (Figures 1 and 2) and those of the singly charged anions (Figure 3). In addition to the difference between their ground-state structures, the very lower electron binding energies observed for $M_2O_7^{2-}$, with respect to $M_2O_7^-$, are primarily due to the intramolecular coulomb repulsion in the dianions. The intramolecular coulomb repulsion also has an important role in the photodetachment processes of the dianions[34] and can be seen more clearly in the photon-energy-dependent studies (see Figures S1−S6 in the Supporting Information). When an electron is removed from a multiply charged anion (A^{n-}), the two photoproducts ($A^{(n-1)-} + e^-$) are both negatively charged. The superposition of the long-range coulomb repulsion between the outgoing electron and the remaining anion and the short-range electron binding produces

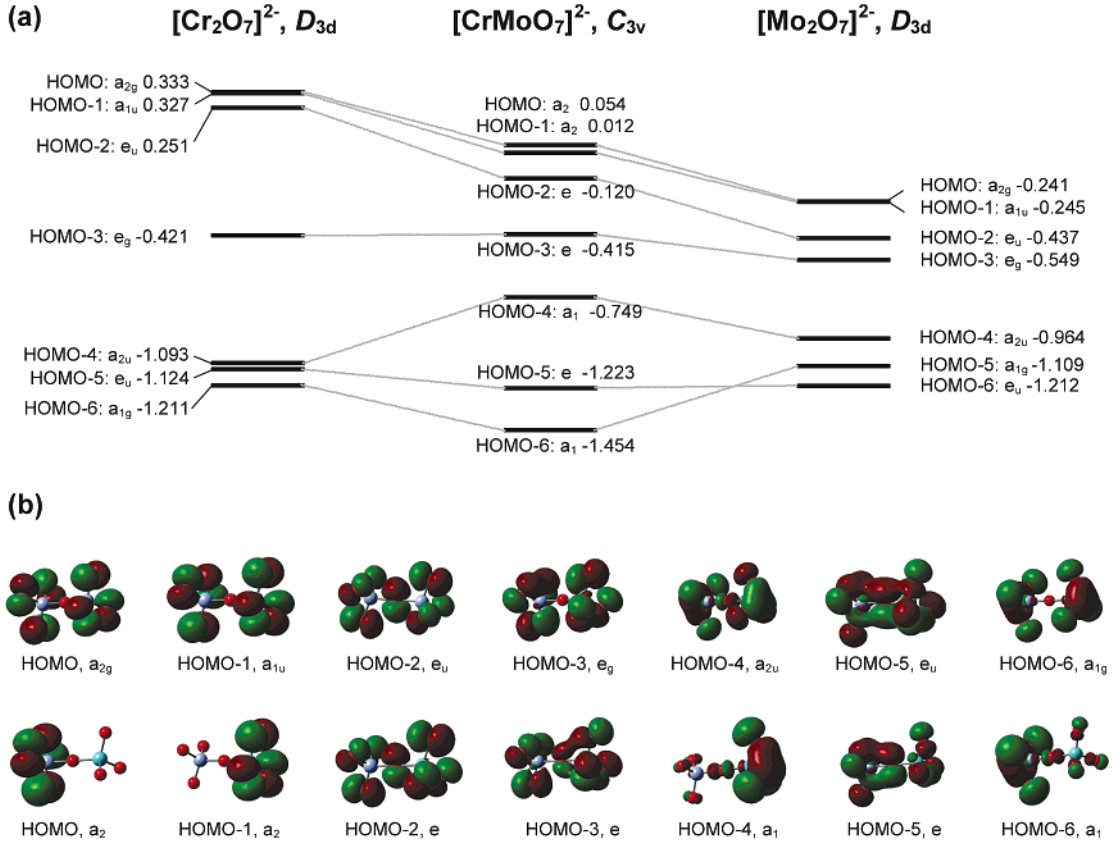

Figure 5. (a) Correlation diagram relating the highest-lying occupied molecular orbitals of $Cr_2O_7^{2-}$, $CrMoO_7^{2-}$, and $Mo_2O_7^{2-}$. Orbital energies (given in units of eV) are relative to the vacuum. (b) Kohn−Sham molecular orbital pictures for the seven highest energy occupied orbitals of $Cr_2O_7^{2-}$ (upper row) and $CrMoO_7^{2-}$ (lower row) (in panel b, the purple color represents Cr and the aqua color represents Mo).

an effective potential barrier for the outgoing electron; this is called the repulsive coulomb barrier (RCB). The RCB prevents slow electrons from being emitted from the multiply charged anions, resulting in spectral cutoffs. We have previously shown that the coulomb repulsion is equal to the magnitude of the RCB, which can be estimated from photon-energy-dependent studies.[35]

The photon-energy-dependent spectra of $M_2O_7^{2-}$ and $MM'O_7^{2-}$ at 157, 193, and 266 nm are given in Figures S1−S6 in the Supporting Information. The 157-nm spectrum of $Cr_2O_7^{2-}$ (Figure 1a and Figure S1c) seemed to be cut off beyond ∼5.5 eV, which indicated an RCB of ∼2.3 eV (7.866−5.5 eV). The onset of cutoff in the 193-nm spectrum (Figure S1b) is observed at ∼4.0 eV, which is consistent with that from the 157-nm spectrum. The spectral cutoff can be seen more clearly in the 266-nm spectrum (Figure S1a), where band B (2.65 eV) is almost completely cutoff. Thus, the 266-nm photon is below the RCB for band B, yielding a lower limit for the RCB as ∼2 eV (4.661 − 2.65 eV). We estimated that the RCB of $Cr_2O_7^{2-}$ should be ∼2.3 eV from the spectral cutoffs at 157, 193, and 266 nm. Similarly, we estimated the RCBs for $Mo_2O_7^{2-}$, $W_2O_7^{2-}$, $CrMoO_7^{2-}$, $CrWO_7^{2-}$, and $MoWO_7^{2-}$ from their photon-energy-dependent spectra (Figures S2−S6) and determined that all six of these dianions possess similar RCBs of ∼2.3 eV within our experimental uncertainty, which is consistent with similar geometrical structures.

Because the negative charges are localized on the terminal O atoms in the $M_2O_7^{2-}$ dianion, we can estimate the intramolecular coulomb repulsion from Coulomb's law. Using the structural parameters given in Figure 4 for $W_2O_7^{2-}$, we obtain an intramolecular coulomb repulsion of ∼2.4 eV, which is remarkably close to the estimated RCB value, confirming again our previous observation that the RCB is equal in magnitude to the intramolecular coulomb repulsion.[35] From Figure 4, we note that the W−O_b distance (1.920 Å) in the ground state of $W_2O_7^{2-}$ **1** is slightly longer than that in the corresponding singly charged $W_2O_7^-$ **2b** (1.905 Å). The intramolecular coulomb repulsion is likely responsible for the lengthening of the W−O_b bonds in the dianion.

6.2. Periodic Changes in Orbital Energies of the Dianions $M_2O_7^{2-}$ (M = Cr, Mo, W). As shown in Figure 1, significant spectral changes were observed from $Cr_2O_7^{2-}$ to $Mo_2O_7^{2-}$, whereas the change from $Mo_2O_7^{2-}$ to $W_2O_7^{2-}$ is relatively small. The trend can be understood from a molecular orbital analysis. Features X, A, and B in the PES spectra of $M_2O_7^{2-}$ (M = Cr, Mo, W) were assigned on the basis of the calculated VDEs (Figure 1 and Table S1 in the Supporting Information). A correlation diagram relating the predicted orbital energies for the relevant orbitals of $Cr_2O_7^{2-}$ and $Mo_2O_7^{2-}$ is given in Figure 5a. The orbital pictures are also illustrated for the $Cr_2O_7^{2-}$ in Figure 5b, whereas the equivalent orbitals for $Mo_2O_7^{2-}$ and $W_2O_7^{2-}$ are very similar.

Our calculations suggest that the HOMO to HOMO-6 levels of $Cr_2O_7^{2-}$ are energetically separated into three distinct groups (Figure 5a), whose binding energies are predicted to occur in the regions of band X, A, and B, respectively (Figure 1a). Accordingly, band X is assigned to detachment from HOMO to HOMO-2, band A to detachment from HOMO-3, and band B from HOMO-4 to HOMO-6. Experimentally, the separations between bands X, A, and B in $Mo_2O_7^{2-}$ are significantly smaller than those in $Cr_2O_7^{2-}$ (Figure 1). This is qualitatively supported by our calculations, which predict a significant reduction in the separation between HOMO to HOMO-6 levels for $Mo_2O_7^{2-}$, resulting from stabilization of its HOMO relative to HOMO-6 (Figure 5a). The PES spectra of $Mo_2O_7^{2-}$ and $W_2O_7^{2-}$ appear

qualitatively similar (Figure 1), which is consistent with the theoretical prediction of similar orbital energies for both species. An equivalent periodic trend was also observed for the monoanions $M_2O_7^-$ (M = Cr, Mo, W), as shown in Figure 3.

6.3. Heteronuclear Dianions $MM'O_7^{2-}$ (M, M′ = Cr, Mo, W). The spectra of the heteronuclear species $MM'O_7^{2-}$ (Figure 2) seemed to be considerably more complex than those of the homonuclear species $M_2O_7^{2-}$ (Figure 1), most likely because of their lower symmetry. The electron binding energies of $MM'O_7^{2-}$ were measured to be roughly the average of those of $M_2O_7^{2-}$ and $M'_2O_7^{2-}$ within the experimental uncertainties (see Table 1). The current observations regarding the electron binding energies of the heteronuclear dianions are consistent with a recent study of their reactivity, which revealed that $MM'O_6(OR)^-$ exhibits reactivity intermediate between that of $M_2O_6(OR)^-$ and $M'_2O_6(OR)^-$.[15]

The orbital energy levels of the seven highest occupied orbitals of $CrMoO_7^{2-}$ are related to those of $Cr_2O_7^{2-}$ and $Mo_2O_7^{2-}$ in the correlation diagram of Figure 5a, whereas the relevant orbital picture is illustrated in Figure 5b. The calculations suggest that the molecular orbital energies of HOMO, HOMO-1, and HOMO-2 for $CrMoO_7^{2-}$ are roughly the average of those of $Cr_2O_7^{2-}$ and $Mo_2O_7^{2-}$, which is in good agreement with the experimental observation. The HOMO-4 and HOMO-6 levels in $Cr_2O_7^{2-}$ and $Mo_2O_7^{2-}$ are of a_{2u} and a_{1g} symmetry, respectively, and are separated by ~0.1 eV in both the Cr and Mo cases. However, for the heteronuclear species, these levels are separated by ~0.5 eV (Figure 5a). The increased splitting predicted for $CrMoO_7^{2-}$ is a result of the lower point symmetry and the fact that these orbitals are localized on the oxo ligands of one metal center: the HOMO-4 is localized on the MoO_3 unit, whereas the HOMO-6 is localized on the CrO_3 unit (see Figure 5b). This increased splitting contributes to the more complex spectrum observed for $CrMoO_7^{2-}$.

6.4. Structural Evolution of $W_2O_7^{2-/-/0}$ as a Function of Charge State. The structural evolution of the species $W_2O_7^{2-/-/0}$, as a function of charge state, is schematically summarized in Figure 6. The DFT calculations locate **1** (D_{3d}, $^1A_{1g}$) as the ground state of $W_2O_7^{2-}$ (see Figure 4). The linear W−O_b−W arrangement in $W_2O_7^{2-}$ is associated with its dianionic nature, where the strong intramolecular Coulomb repulsion results in maximum separation of the charges and a linear arrangement. The bridging oxo angle in the solid compounds of $Cr_2O_7^{2-}$ and $Mo_2O_7^{2-}$ is observed to vary as a function of counterion: linear $Mo_2O_7^{2-}$ dianions were observed in several compounds,[7] although, in other compounds, the $Mo_2O_7^{2-}$ dianions adopt bent structures with the ∠MoO_bMo angle ranging from 153° to 160°.[6] Recent DFT calculations on $Cr_2O_7^{2-}$ showed that the potential energy surface, with respect to the bending angle, is remarkably flat (<1 kcal/mol higher for ∠CrO_bCr = 180° than the minimum at ∠CrO_bCr = 150°).[5] Although it does not exist in the condensed phase, the $W_2O_7^{2-}$ dianion can be produced by the ESI process (see Figure 1c). Upon photodetachment, the linear $W_2O_7^-$ (**2b**) monoanion should be reached. The experimental VDE for the **2b** ← **1** transition (~2.3 eV, Table 1) is in good agreement with the calculated VDE of 1.97 eV.

Linear structures of $W_2O_7^-$ (**2b**) monoanion and W_2O_7 (**3b**) neutral are also minima but are 0.09 and 0.66 eV higher in energy than their corresponding ground-state structures **2a** and **3a**. The W−O_b−W arrangement is linear in $W_2O_7^{2-}$ (**1**) and $W_2O_7^-$ (**2b**) but slightly bent in neutral W_2O_7 (**3b**). The unpaired electron in the linear $W_2O_7^-$ (**2b**) is delocalized over the terminal oxo ligands of both metal centers. In contrast, the related structure on the neutral potential energy surface (**3b**) is predicted

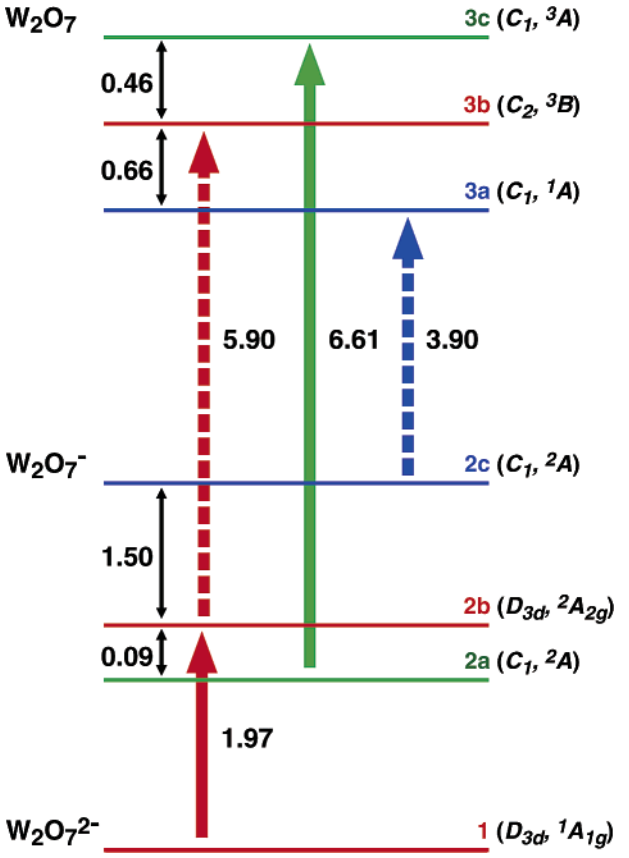

Figure 6. Schematic diagram showing the energetic relationship between $W_2O_7^{2-}$, $W_2O_7^-$, and W_2O_7. Different conformers are shown in different colors, and three types of conformers are shown for $W_2O_7^-$ and W_2O_7. All structures are labeled as shown in Figure 4, and all energies (given in units of eV) are from theoretical calculations. Solid thick arrows indicate transitions that were accessed in the current photodetachment experiments.

to be a triplet with two terminal radical oxo ligands—one on each metal center.

The ground state of the monoanion $W_2O_7^-$ **2a** (C_1, ^2A) contains two bridging oxo ligands and a radical oxo ligand. The extra charge is localized on the terminal oxo ligand with a longer W−O_t bond. Upon photodetachment from $W_2O_7^-$ (**2a**), the **3c** (C_1, ^3A) neutral state is reached (Figure 6), which is a triplet state and 1.12 eV above the ground state (**3a**). Similar to the W_2O_7 **3b** isomer, the W_2O_7 **3c** species also contains two radical oxo ligands; however, in the latter, these are located at the same tungsten center. From Figure 6, one can see easily that the global minimum structure of $W_2O_7^-$ **2a** yields the highest VDE, relative to the **2b** or **2c** low-lying structures. The high VDE of **2a** agrees well with the experimental PES data, confirming it to be the global minimum for $W_2O_7^-$.

The ground state of the W_2O_7 neutral is **3a** (C_1, ^1A), which is 0.66 and 1.12 eV lower in energy than **3b** and **3c**, respectively (see Figure 4). This isomer can be viewed by replacing a terminal oxo ligand of the D_{2d} stoichiometric W_2O_6 species[36] by a peroxo ligand. The W_2O_6 species is a thermodynamically stable vapor species,[37] for which recent anion PES studies revealed an extremely large HOMO−LUMO gap of ~2.8 eV.[16c,36] Our calculations suggest that the lowest unoccupied molecular orbital (LUMO) of W_2O_7 **3a** is metal based, similar to that of the parent W_2O_6.[36] Electron attachment to the W_2O_7 **3a** neutral would result in the $W_2O_7^-$ **2c** monoanion, with the extra electron entering into the W 5d-based orbital, i.e., the LUMO of neutral W_2O_7 **3a**. The calculated VDE for the **3a** ←

2c transition is 3.90 eV (Figure 6), which is similar to the VDE of 3.63 eV for $W_2O_6^-$,[36] but much lower than the experimental value of the ground-state $W_2O_7^-$ **2a** (6.7 eV). This suggests that the $W_2O_7^-$ **2c** isomer is not accessed in the present experiment, which is consistent with it being 1.59 eV above the ground-state $W_2O_7^-$ (**2a)**. Thus, Figure 6 outlines a unique electronic system comprising three charge states for W_2O_7 and seven distinct chemical species. Each charge state exhibits a different ground-state conformation: **1**, **2a**, and **3a** for the doubly charged, singly charged, and neutral species, respectively.

7. Conclusions

We report the investigation of a series of dinuclear Group VIB oxometalate dianions and monoanions using photoelectron spectroscopy and density functional calculations. It is rare that various charge states of the same species can be studied in the gas phase. In the present work, we produced these species using two different experimental techniques. We generated the dianions, $M_2O_7^{2-}$ and $MM'O_7^{2-}$ (M = Cr, Mo, W), using electrospray ionization and the corresponding homonuclear $M_2O_7^-$ monoanions using laser vaporization. Photodetachment experiments revealed that $M_2O_7^{2-}$ and $MM'O_7^{2-}$ dianions are stable gas-phase species with positive electron binding energies, despite the strong intramolecular Coulomb repulsion. The electron binding energies were observed to increase significantly from $Cr_2O_7^{2-}$ to $Mo_2O_7^{2-}$, but only marginally from $Mo_2O_7^{2-}$ to $W_2O_7^{2-}$. The electron binding energies for the heteronuclear dianions $MM'O_7^{2-}$ were observed to be approximately the average of those for their homonuclear counterparts $M_2O_7^{2-}$ and $M'_2O_7^{2-}$. The $M_2O_7^-$ monoanions were all observed to possess very high electron binding energies (>5.5 eV), indicating that their corresponding neutral M_2O_7 species should be strong oxidizers. The photoelectron spectra of the dianions were compared with the calculated vertical electron detachment energies (VDEs). The periodic trend of the PES spectra of the dianions from Cr to W was understood using molecular orbital analyses. Density functional calculations established that the different charge states $W_2O_7^{2-}$, $W_2O_7^-$, and W_2O_7 each possess a distinctly different global minimum structure. Low-lying isomers for $W_2O_7^-$ and W_2O_7 were also located and two different isomers were accessed for $W_2O_7^-$: a D_{3d} isomer as the final state of photodetachment from the D_{3d} $W_2O_7^{2-}$ and the dibridged global minimum structure generated from the laser vaporization experiment. The electronic and structural information presented should be valuable to understand the chemical and catalytic properties of these Group VIB dinuclear oxometalate dianions, monoanions, and their neutral counterparts.

Acknowledgment. We thank Dr. Jun Li for valuable discussions. This work was supported by the Chemical Sciences, Geosciences and Biosciences Division, Office of Basic Energy Sciences, U.S. Department of Energy (DOE), under Grant No. DE-FG02-03ER15481 (Catalysis Center Program) and was performed at the W. R. Wiley Environmental Molecular Sciences Laboratory (EMSL), which is a national scientific user facility sponsored by DOE's Office of Biological and Environmental Research and located at Pacific Northwest National Laboratory, operated for DOE by Battelle. The Australian Research Council is thanked for financial support under Grant No. A00103008. Calculations were performed on the EMSL Molecular Science Computing Facility, as well as the Victorian Institute for Chemical Sciences High Performance Computing Facility.

Supporting Information Available: Photon-energy-dependent photoelectron spectra of dimetalate dianions $M_2O_7^{2-}$ and $MM'O_7^{2-}$ (M, M′ = Cr, Mo, W) at 266, 193, and 157 nm, and computational VDEs of $Cr_2O_7^{2-}$, $Mo_2O_7^{2-}$, $CrMoO_7^{2-}$, $W_2O_7^{2-}$, and $W_2O_7^-$ determined using the generalized Koopman's theorem and tentative assignment of the photoelectron spectra (PDF). These materials are available free of charge via the Internet at http://pubs.acs.org.

References and Notes

(1) (a) Pope, M. T. *Heteropoly and Isopoly Oxometalates*; Springer−Verlag: Berlin, 1983. (b) Pope, M. T.; Muller, A. *Angew. Chem., Int. Ed. Engl*. **1991**, *30*, 34. (c) For a recent special issue on polyoxometalates, see: Hill, C. L., Ed. *Chem. Rev.* **1998**, *98*, 1−387.

(2) (a) Ertl, G., Knözinger, H., Weitkamp, J., Eds. *Handbook of Heterogeneous Catalysis*; Wiley: Weinheim, Germany, 1997, 2541 pp. (b) Rao, C. N. R.; Raveau, B. *Transition Metal Oxides: Structure, Properties and Synthesis of Ceramic Oxides*, 2nd Edition; Wiley−VCH: Weinheim, Germany, 1998; 373 pp.

(3) (a) Wang, S.; Murata, K.; Hayakawa, T.; Hamakawa, S.; Suzuki, K. *Catal. Lett.* **2000**, *66*, 13. (b) Jibril, B. Y.; Al-Zahrani, S. M.; Abasaeed, A. E.; Hughes, R. *Catal. Commun.* **2003**, *4*, 579.

(4) (a) Stammreich, H.; Bassi, D.; Sala, O.; Siebert, H. *Spectrochim. Acta* **1958**, *13*, 192. (b) Scheuermann, W.; Ritter, G. J. *J. Mol. Struct.* **1970**, *6*, 240. (c) Radhakrishna, S.; Sharma, B. D. *J. Chem. Phys.* **1974**, *61*, 3925. (d) Dave, B. C.; Czernuszewicz, R. S. *Inorg. Chem.* **1994**, *33*, 847. (e) Norquist, A. J.; Heier, K. R.; Halasyamani, P. S.; Stern, C. L.; Poeppelmeier K. R. *Inorg. Chem.* **2001**, *40*, 2015.

(5) Lorenzo, S.; Craig, D. C.; Scudder, M. L.; Dance, I. G. *Polyhedron* **1999**, *18*, 3181.

(6) (a) Stadnicka, K.; Haber, J.; Kozlowski, R. *Acta Crystallogr. B* **1977**, *33*, 3859. (b) Day, V. W.; Fredrich, M. F.; Klemperer, W. G.; Shum, W. *J. Am. Chem. Soc.* **1977**, *99*, 6146. (c) Gatehouse, B. M.; Same, R. *J. Solid State Chem.* **1978**, *25*, 115. (d) Braunstein, P.; Bellefon, C. M.; Lanfranchi, M.; Tiripicchio, A. *Organometallics* **1984**, *3*, 1772. (e) Griffith, W. P.; Nogueira, H. I. S.; White, A. J. P.; Williams, D. J. *Polyhedron* **1997**, *16*, 1323.

(7) (a) Becher, H. J.; Fenske, D. *J. Chem. Res.* **1978**, 167. (b) Naruke, H.; Yamase, T. *J. Solid State Chem.* **2005**, *178*, 702.

(8) Gatehouse, B. M.; Leverett, P. *J. Chem. Soc., Dalton Trans*. **1976**, 1316.

(9) Gatehouse, B. M.; Jozsa, A. J. *J. Solid State Chem.* **1987**, *71*, 34.

(10) (a) Errington, R. J.; Kerlogue, M. D.; Richards, D. G. *Chem. Commun.* **1993**, 649. (b) Clegg, W.; Errington, R. J.; Fraser, K. A.; Richards, D. G. *Chem. Commun.* **1993**, 1105.

(11) (a) Okada, K.; Morikawa, H.; Marumo, F.; Iwai, S. *Acta Crystallogr. B* **1975**, *31*, 1200. (b) Okada, K.; Morikawa, H.; Marumo, F.; Iwai, S. *Acta Crystallogr. B* **1975**, *31*, 1451. (c) Range, K. J.; Haase, H. *Acta Crystallogr. C* **1990**, *46*, 317. (d) Brudgam, I.; Fuchs, J.; Hartl, H.; Palm, R. *Angew. Chem., Int. Ed. Engl.* **1998**, *37*, 2668. (e) Dahlborg, M. A.; Svensson, G.; Valkeapaa, M. *J. Solid State Chem.* **2002**, *167*, 525.

(12) (a) Lau, T. C.; Wang, J.; Siu, K. W. M.; Guevremont, R. *J. Chem. Soc. Chem. Commun.* **1994**, 1487. (b) Lau, T. C.; Wang, J.; Guevremont, R.; Siu, K. W. M. *J. Chem. Soc. Chem. Commun.* **1995**, 877. (c) Walanda, D. K.; Burns, R. C.; Lawrance, A.; Nagy-Felsobuki, E. I. *J. Chem. Soc., Dalton Trans.* **1999**, 311.

(13) Waters, T.; O'Hair, R. A. J.; Wedd, A. G. *J. Am. Chem. Soc.* **2003**, *125*, 3384.

(14) (a) Deery, M. J.; Howarth, O. W.; Jennings, K. R. *J. Chem. Soc., Dalton Trans.* **1997**, 4783. (b) Truebenbach, C. S.; Houalla, M.; Hercules, D. M. *J. Mass. Spectrom.* **2000**, *35*, 1121.

(15) Waters, T.; O'Hair, R. A. J.; Wedd, A. G. *Inorg. Chem.* **2005**, *44*, 3356.

(16) (a) Hachimi, A.; Poitevin, E.; Krier, G.; Miller, J. F.; Ruiz-Lopez, M. F. *Int. J. Mass Spectrom. Ion Process*. **1995**, *144*, 23. (b) Gianotto, A. K.; Hodges, B. D. M.; Harrington, P. B.; Appelhans, A. D.; Olson, J. E.; Groenewold, G. S. *J. Am. Soc. Mass Spectrom.* **2003**, *14*, 1067. (c) Sun, Q.; Rao, B. K.; Jena, P.; Stolcic, D.; Kim, Y. D.; Gentefor, G. *J. Chem. Phys.* **2004**, *121*, 9417.

(17) (a) Amado, A. M.; Ribeiro-Claro, P. L. A. *J. Mol. Struct. (THEOCHEM)* **1999**, *469*, 191. (b) Bridgeman, A. J.; Cavigliasso, G. *J. Phys. Chem. A* **2001**, *105*, 7111.

(18) (a) Mestres, J.; Duran, M.; Martin-Zarza, P.; Rosa, E. M.; Gili, P. *Inorg. Chem.* **1993**, *32*, 4708. (b) Bell, S.; Dines, T. J. *J. Phys. Chem. A* **2000**, *104*, 11403. (c) Bridgeman, A. J.; Cavigliasso, G. *J. Phys. Chem. A* **2003**, *107*, 4568.

(19) Zhai, H. J.; Kiran, B.; Cui, L. F.; Li, X.; Dixon, D. A.; Wang, L. S. *J. Am. Chem. Soc.* **2004**, *126*, 16134.

(20) Yang, X.; Waters, T.; Wang, X. B.; O'Hair, R. A. J.; Wedd, A. G.; Li, J.; Dixon, D. A.; Wang, L. S. *J. Phys. Chem. A* **2004**, *108*, 10089.

(21) Zhai, H. J.; Wang, L. S. *J. Chem. Phys*. **2005**, *122*, 051101.

(22) For a recent review, see: Bohme, D. K.; Schwarz, H. *Angew. Chem., Int. Ed.* **2005**, *44*, 2336.

(23) Zemski, K. A.; Justes, D. R.; Castleman, A. W., Jr. *J. Phys. Chem. B* **2002**, *106*, 6136.

(24) (a) Shi, Y.; Ervin, K. M. *J. Chem. Phys.* **1998**, *108*, 1757. (b) Sanchez, A.; Abbet, S.; Heiz, U.; Schneider, W. D.; Hakkinen, H.; Barnett, R. N.; Landman, U. *J. Phys. Chem. A* **1999**, *103*, 9573. (c) Wallace, W. T.; Whetten, R. L. *J. Am. Chem. Soc.* **2002**, *124*, 7499. (d) Socaciu, L. D.; Hagen, J.; Bernhardt, T. M.; Woste, L.; Heiz, U.; Hakkinen, H.; Landman, U. *J. Am. Chem. Soc.* **2003**, *125*, 10437. (e) Stolcic, D.; Fischer, M.; Gantefor, G.; Kim, Y. D.; Sun, Q.; Jena, P. *J. Am. Chem. Soc.* **2003**, *125*, 2848. (f) Justes, D. R.; Mitric, R.; Moore, N. A.; Bonacic-Koutecky, V.; Castleman, A. W., Jr. *J. Am. Chem. Soc*. **2003**, *125*, 6289.

(25) Wang, L. S.; Ding, C. F.; Wang, X. B.; Barlow, S. E. *Rev. Sci. Instrum.* **1999**, *70*, 1957.

(26) (a) Wang, L.S.; Cheng, H. S.; Fan, J. *J. Chem. Phys*. **1995**, *102*, 9480. (b) Wang, L. S.; Wu, H. In *Advances in Metal and Semiconductor Clusters. IV. Cluster Materials*; Duncan, M. A., Ed.; JAI: Greenwich, CT, 1998; pp 299−343.

(27) (a) Becke, A. D. *J. Chem. Phys*. **1993**, *98*, 1372, 5648. (b) Lee, C.; Yang, W.; Parr, R. G. *Phys. Rev. B* **1988**, *37*, 785. (c) Stephens, P. J.; Devlin, F. J.; Chabalowski, C. F.; Frisch, M. J. *J. Phys. Chem*. **1994**, *98*, 11623.

(28) (a) Andrae, D., Haeussermann, U., Dolg, M., Stoll, H., Preuss, H. *Theor. Chim. Acta* **1990**, *77*, 123. (b) Kuchle, W.; Dolg, M.; Stoll, H.; Preuss, H. *Pseudopotentials of the Stuttgart/Dresden Group 1998 Revision*, August 11, 1998 (available via the Internet at http://www.theochem.uni-stuttgart.de/pseudopotentiale).

(29) Martin, J. M. L.; Sundermann, A. *J. Chem. Phys*. **2001**, *114*, 3408.

(30) (a) Dunning, T. H., Jr. *J. Chem. Phys*. **1989**, *90*, 1007. (b) Kendall, R. A.; Dunning, T. H., Jr.; Harrison, R. J. *J. Chem. Phys*. **1992**, *96*, 6796.

(31) Tozer, D. J.; Handy, N. C. *J. Chem. Phys*. **1998**, *109*, 10180.

(32) *NWChem, A Computational Chemistry Package for Parallel Computers, Version 4.6*, Pacific Northwest National Laboratory, Richland, WA, 2004.

(33) Extensible Computational Chemistry Environment, available via the Internet at http://ecce.emsl.pnl.gov/.

(34) (a) Wang, L. S.; Wang, X. B. *J. Phys. Chem. A* **2000**, *104*, 1978. (b) Wang, X. B.; Wang, L. S. *Nature* **1999**, *400*, 245. (c) Wang, X. B.; Ding, C. F.; Wang, L. S. *Chem. Phys. Lett.* **1999**, *307*, 391.

(35) (a) Wang, L. S.; Ding, C. F.; Wang, X. B.; Nicholas, J. B. *Phys. Rev. Lett.* **1998**, *81*, 2667. (b) Wang, X. B.; Nicholas, J. B.; Wang, L. S. *J. Chem. Phys.* **2000**, *113*, 653.

(36) Zhai, H. J.; Huang, X.; Cui, L. F.; Li, X.; Li, J.; Wang, L. S. *J. Phys. Chem. A* **2005**, *109*, 6019.

(37) Ackermann, R. J.; Rauh, E. G. *J. Phys. Chem*. **1963**, *67*, 2596.